On the micromechanics of liquefaction in granular materials

S. A. Galindo-Torres,[1,2,*] X. Zhang,[1] and K. Krabbenhoft[1]

[1] *Department of Civil Engineering and Industrial Design, School of Engineering, University of Liverpool UK*

[2] *Geotechnical Engineering Centre. School of Civil Engineering, The University of Queensland, Brisbane QLD 4072, Australia*

In this paper a Discrete Element Method (DEM) implementation is developed to study the micromechanics of liquefaction in granular materials. In a liquefaction event, the pore water acts as a cushion between the grains, reducing the contact and friction forces and the overall soil strength. The proposed model reproduces this phenomenon by introducing the effect of pore water as a constraint over the DEM particles' mechanics. The DEM particles will suffer resistance to any displacement changing the pore volume, which takes into account the very small compressibility of water. It is found that this constraint is enough to simulate soil liquefaction under quasistatic deformation. Lastly, it is shown that the initial density of the granular skeleton, defined by the number of contacts between grains, plays a critical role in determining if the soil will liquefy or not. This critical value opens for the possibility of treating liquefaction in soils as a bifurcation problem.

I. INTRODUCTION

Liquefaction in soils is a hazardous phenomenon occurring when the pores within the granular packing are fully saturated with water. The behaviour of all saturated granular materials will, to a smaller or greater extent, be affected by the excess pore pressures that tend to be generated in response to loading. The exact effect of the excess pore pressures on the overall response depends on both the permeability of the material relative to the rate of loading and on the material's tendency to contract or dilate. For coarse grained soils such as sand and gravel, the permeability is such that the excess pore pressures that would tend to be generated in response to loading, dissipate before attaining a magnitude that affects the overall response of the material. Such conditions are typically referred to as 'drained'. For fine grained materials such as clays, the permeability may be such that significant excess pore pressures build up and only dissipate slowly with time. For such materials, the state immediately after application of the load and before any significant dissipation of excess pore pressure is referred to as 'undrained'. Moreover, for very loose sands that tend to compact significantly in response to shearing, pore pressures of a magnitude sufficient to affect the overall behavior significantly may be generated even under small rates of loading. In this case, when the soil is sheared, the water will effectively act as a cushion between the grains, absorbing the applied pressure and reducing the friction forces at the solid phase. With sufficient reduction, the soil is unable to sustain any shear stress. At this point the soil behaves like a liquid, becoming liquefied [1]. Liquefaction is a critical hazard in the field of Civil Engineering where soils losing strength due to shearing may be the origin of collapses in foundations, slopes, dams, etc.

* s.torres@liverpool.ac.uk

To illustrate the liquefaction effect graphically it is useful to describe the soil shearing process under undrained conditions in terms of the following quantities:

$$p' = \frac{\sigma'_1 + \sigma'_2 + \sigma'_3}{3}, \tag{1}$$

$$q = \frac{\sqrt{(\sigma_1 - \sigma_2)^2 + (\sigma_2 - \sigma_3)^2 + (\sigma_3 - \sigma_1)^2}}{\sqrt{2}}, \tag{2}$$

where σ_i are the principal stresses, $\sigma'_i = \sigma_i - u$, with u being the pore pressure, are the so-called effective stresses, p' is the effective mean stress and q is the deviatoric stress [2]. Fig. 1 shows a typical soil shearing process for three types of soils with different packing densities, from loose to dense. The soils are initially compressed isotropically ($q = 0$) from a zero stress state. Then, after reaching a given mean stress, the soil is sheared, increasing the deviatoric stress.

Denser soils follow a path where both p' and q, owing to a tendency to dilation, continue to increase. In contrast, loose soils follows a path where both p' tends to decrease somewhat owing to a limited amount tendency to contraction. For very loose soils, this tendency to contraction may be such that p' eventually becomes zero. At this point the soil is liquefied. The three trajectories all tend to converge to the critical state line (CSL)[3] which defines the strength envelope.

Loose or dense soils are relative concepts, and most criteria used in Civil Engineering to classify them are empirical in nature. Despite a less than rigorous definition, it is clear from Fig. 1 that relative density plays a critical role in the bifurcation of the different paths the soil follows during undrained shearing. Such a strong bifurcation, commonly found in problems that are sensitive to initial conditions and therefore chaotic, makes predicting liquefaction a daunting task for the soil scientist.

This paper introduces a micromechanical model to study the liquefaction phenomenon. It is based on the commonly used Discrete Element Method [4] (DEM) to

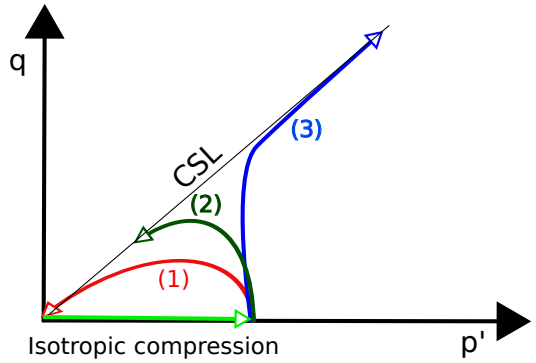

Figure 1. q vs p' showing the difference between different soil samples during undrained shearing. Sample (1) suffers a complete collapse of the soil strength, signalling soil liquefaction. Sample (2) suffers limited decrease of p' with q. This happens for loose sands as a result of a limited amount of compaction. Finally, for sample (3), both p' and q increase while tending to the CSL.

model micromechanically soils and rocks [5, 6]. DEM has been used before to model soil shearing during undrained conditions [1, 7]. However, in these studies, the undrained condition is imposed macroscopically by keeping a constant volume in the simulated experimental test. As explained before, liquefaction occurs at the grain scale, and therefore a microscopic law is introduced to keep the pore volume constant during shearing. It will be shown that the model is able to reproduce the behaviour of Fig. 1 and it also gives important information about the physics occurring at the grain scale.

In Sec. II the mathematical foundation of the model is introduced and the effect of some parameters is presented to see where the behaviour of Fig. 1 is reproduced. Sec. III shows some results for different soils sheared under undrained conditions. In this section, observations of the mechanics at the pore scale are also presented. Finally, Sec. IV presents the conclusions and predictions of the model.

II. THE MODEL

As mentioned in the introduction, the foundation of the model is based on DEM. DEM describes the soil as a discrete set of particles with their dynamics ruled by Newton's laws which are integrated numerically [8] for both translational and rotational degrees of freedom. To detect a collision, at each time step the overlapping of the particles δ, as seen in Fig. 2 is checked and a linear dashpot law is imposed to calculate the force F_n between the colliding particles,

$$\vec{\boldsymbol{F}}_n = K_n \delta \hat{\boldsymbol{n}}, \tag{3}$$

where K_n is a normal stiffness constant characterizing the deformation of the material and $\hat{\boldsymbol{n}}$ is defined as the normal unit vector at the plane of contact, parallel to the line joining the sphere centres (Fig. 2).

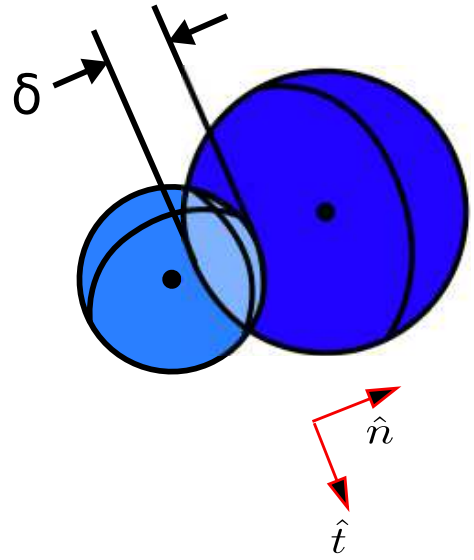

Figure 2. Collision of two spheres calculated as a spring proportional to the overlapping distance δ.

Viscous forces $\vec{\boldsymbol{F}}_v$ are introduced to dissipate energy during the collision in a normal direction. Such forces are proportional to the relative normal velocity between the particles $\vec{\boldsymbol{v}}_n$ as,

$$\vec{\boldsymbol{F}}_v = -m_e \gamma_n \vec{\boldsymbol{v}}_n, \tag{4}$$

with m_e the reduced mass of the particle pair and γ_n a viscosity constant, which depends on the restitution coefficient e as [9],

$$e = \exp\left(-\frac{\gamma_n}{2} \frac{\pi}{\sqrt{\frac{K_n}{m_e} - \left(\frac{\gamma_n}{2}\right)^2}} \right) \tag{5}$$

Frictional forces $\vec{\boldsymbol{F}}_f$ are introduced by keeping track of the tangential relative displacement $\vec{\boldsymbol{\xi}}$ which is the time integration of the relative tangential velocity $\vec{\boldsymbol{v}}_t$ (i.e. $\vec{\boldsymbol{\xi}} = \int \vec{\boldsymbol{v}}_t dt$). The frictional force follows the following formula,

$$\vec{\boldsymbol{F}}_f = -\min(K_t \xi, \mu F_n) \hat{\boldsymbol{t}}, \tag{6}$$

where μ is the friction coefficient, K_t is a tangential stiffness and $\hat{\boldsymbol{t}}$ is the tangential vector in the contact plane (Fig. 2) which is always parallel to $\vec{\boldsymbol{v}}_t$.

Finally, a rolling resistance model is also introduced to the DEM formulation to represent the effect of non-spherical shapes in real grains. Perfect spheres can always roll, mitigating the effect of frictional forces, whereas real grains will always have a resistance to rolling due to the shape [10]. To introduce the rolling resistance model used in this study, first the rolling displacement $\vec{\boldsymbol{\xi}}_r$

is defined as the time integration of the objective rolling velocity $\vec{\boldsymbol{v}}_r$ (i.e. $\vec{\boldsymbol{\xi}}_r = \int \vec{\boldsymbol{v}}_r dt$). This velocity is defined as [11],

$$\vec{\boldsymbol{v}}_r = R_e(\vec{\boldsymbol{\omega}}_1 - \vec{\boldsymbol{\omega}}_2) \times \hat{\boldsymbol{n}}, \tag{7}$$

where $\vec{\boldsymbol{\omega}}_{1,2}$ is the angular velocity vector of each of the spheres in contact and R_e is the effective radius of the pair. With the rolling displacement, a rolling resistant force $\vec{\boldsymbol{F}}_r$ is defined as,

$$\vec{\boldsymbol{F}}_r = -\min(\beta K_t \xi_r, \eta\mu F_n)\frac{\vec{\boldsymbol{v}}_r}{v_r}, \tag{8}$$

with β the rolling resistance stiffness coefficient and η is the plastic moment coefficient. This force, in turn, produces a rolling resistance torque $\vec{\boldsymbol{\tau}}_r$ defined as,

$$\vec{\boldsymbol{\tau}}_r = R\hat{\boldsymbol{n}} \times \vec{\boldsymbol{F}}_r. \tag{9}$$

This torque is the one introduced into the equations of motion for the particles. Once all the forces and torques are added, the equations of movement are numerically integrated. The presented DEM formulation has been validated before with experimental data [12, 13] and is included in the Mechsys open source multi-physics simulation library [14].

The second part of the model is the introduction of the effect of water for undrained shearing conditions. In order to do this, the pore space between contacting grains is divided into a Delaunay tessellation. For this stage, the CGAL library was used [15]. Undrained conditions are imposed by adding forces, applied to the nodes (DEM particles), resisting volume changes (Fig. 3). In order to deduce such forces, a continuum mechanics approach is taken for the pore water, as it is usually the case for Finite Element Analysis (FEA) [16] in its weak form. The first equation comes from the conservation of momentum,

$$\nabla^T \boldsymbol{\sigma} = \nabla^T(\boldsymbol{I}u) = \vec{\boldsymbol{0}}^T \tag{10}$$

$$\nabla^T(\boldsymbol{I}u) \cdot \vec{\boldsymbol{m}} = 0, \tag{11}$$

where $\boldsymbol{\sigma} = u\boldsymbol{I}$ and $\boldsymbol{I}$ are the stress and identity tensors, $\vec{\boldsymbol{m}}^T = (1,1,1)$ and u is the pore pressure. In this equation, it has been assumed that the pore space is an isotropic material unable to sustain any shear stresses and the stress tensor is diagonal. Viscous and inertial forces are also ignored since the goal is to simulate quasi-static conditions were these forces are negligible. This are the desired properties to represent pore water for this study.

By multiplying Eq. 11 the displacement vector $\widetilde{\boldsymbol{s}}^T = (\Delta x_1, \Delta y_1, \Delta z_1, \Delta x_2, ...)$ (a transposed vector with 12 components, 3 for each node),

$$\widetilde{\boldsymbol{s}}^T \nabla^T(\boldsymbol{I}u) \cdot \vec{\boldsymbol{m}} = \widetilde{\boldsymbol{0}}, \tag{12}$$

and then integrating over the element volume V the following equation is obtained,

$$\int_V \widetilde{\boldsymbol{s}}^T \nabla^T(\boldsymbol{I}u) \cdot \vec{\boldsymbol{m}}\, dV = \widetilde{\boldsymbol{0}}. \tag{13}$$

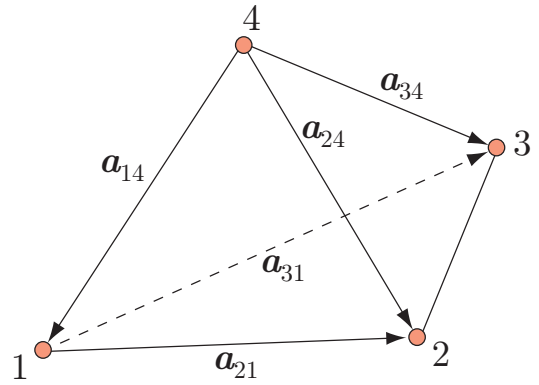

Figure 3. A single pore, represented as a tetrahedron with nodes positioned at the center of 4 DEM particles in contact. The vectors $\vec{\boldsymbol{a}}_{ij}$ connecting different node pairs are used in the development of the mathematical constraint.

Integrating this by parts, and using the divergence theorem to turn the volume integral into a surface integral, an equation for the force vector $\widetilde{\boldsymbol{f}}$ (a 12 component vector) over the nodes is obtained,

$$\widetilde{\boldsymbol{s}}^T \widetilde{\boldsymbol{f}} = \int_V (\nabla^T \widetilde{\boldsymbol{s}} \cdot \vec{\boldsymbol{m}})(u) dV. \tag{14}$$

At this point, a FEA approximation is taken [17] for the differential operators,

$$(\nabla^T \widetilde{\boldsymbol{s}} \cdot \vec{\boldsymbol{m}}) \approx \widetilde{\boldsymbol{s}}^T \boldsymbol{B}^T \cdot \vec{\boldsymbol{m}}, \tag{15}$$

where $\boldsymbol{B}$ is a shape function of the form,

$$\boldsymbol{B}^T = \frac{1}{6V}\begin{bmatrix} n_x^1 & 0 & 0 & n_x^2 & 0 & 0 & n_x^3 & 0 & 0 & n_x^4 & 0 & 0 \\ 0 & n_y^1 & 0 & 0 & n_y^2 & 0 & 0 & n_y^3 & 0 & 0 & n_y^4 & 0 \\ 0 & 0 & n_z^1 & 0 & 0 & n_z^2 & 0 & 0 & n_z^3 & 0 & 0 & n_z^4 \end{bmatrix}, \tag{16}$$

that depends on the normal vectors (Fig. 3),

$$\begin{aligned} \vec{\boldsymbol{n}}^1 &= \vec{\boldsymbol{a}}_{24} \times \vec{\boldsymbol{a}}_{34} \\ \vec{\boldsymbol{n}}^2 &= \vec{\boldsymbol{a}}_{34} \times \vec{\boldsymbol{a}}_{14} \\ \vec{\boldsymbol{n}}^3 &= \vec{\boldsymbol{a}}_{14} \times \vec{\boldsymbol{a}}_{24} \\ \vec{\boldsymbol{n}}^4 &= \vec{\boldsymbol{a}}_{21} \times \vec{\boldsymbol{a}}_{31}. \end{aligned} \tag{17}$$

The 12-component force vector is reduced to,

$$\widetilde{\boldsymbol{f}} = \frac{1}{6}\widetilde{\boldsymbol{N}}u, \tag{18}$$

where $\widetilde{\boldsymbol{N}} = \boldsymbol{B}^T \cdot \vec{\boldsymbol{m}} = (n_x^1, n_y^1, n_z^1, n_x^2, ...)$. From this, the force $\vec{\boldsymbol{F}}^i$ over each one of the DEM particles can be formulated as,

$$\vec{\boldsymbol{F}}^i = \frac{1}{6}\vec{\boldsymbol{n}}^i u. \tag{19}$$

which is proportional to the pore pressure and goes in the direction of the normal vector opposite to the corresponding node. This is an important feature of the model

Constant	Description
$K_n = 1.0$ MN/m	Contact normal stiffness
$K_t = 1.0$ MN/m	Contact tangential stiffness
$\mu_0 = 0.0 - 0.2$	Microscopic friction coefficient for the isotropic compression stage
$\mu = 0.2$	Microscopic friction coefficient for the undrained shearing stage
$e = 0.2$	Restitution coefficient
$\beta = 0.12$	Rolling resistance stiffness coefficient
$\eta = 1.0$	Plastic moment coefficient

Table I. Microscopic constants for the DEM simulations.

since any translation of the node that is tangential to the opposite face will not change the element volume. Only translations that are normal to the opposite face change the pore volume and these forces oppose such change.

The final element of the model is the constitutive relation for the pore pressure u. It is assumed that the pore water is compressible and characterized by a bulk modulus K_w. The linear constitutive relation assumed in this study is,

$$u = -K_w \frac{\Delta V}{V} = -K_w \epsilon_v, \tag{20}$$

and so the pore pressure is proportional to the volumetric strain ϵ_v. If the volume is reduced, the pressure is positive and the forces will work towards expanding the tetrahedral element and vice-versa. These new forces are added to the net force of each particle before the integration step [13].

A triaxial test was programmed by enclosing an ensemble of DEM spheres within six rigid walls as seen in Fig. 4. 14000 spheres of random radii R varying from 0.45 to 0.9mm and density $\rho = 3000\text{kg/m}^3$ were taken as the granular sample. The length size of the triaxial cubic cell is approximately 2cm (it changes slightly as the sample is sheared), so any pressure gradient produced by gravity can be ignored. The sample parameters are included in Table I. The triaxial tests by compressing the sample isotropically with a pressure of 5kPa. Then the shearing stage starts by moving the lids in one direction with a constant strain rate $\dot{\epsilon}_z$ while keep applying isotropic pressure on the other two directions. This is the "3 to 1" stress path, so called because of $\Delta q/\Delta p = 3$ [2]. At this stage is important to ensure quasistatic conditions by keeping the inertial number $I = \dot{\epsilon}_z R\sqrt{\rho/p}$ close to 0.001 [18], which gives an upper boundary for the value of $\dot{\epsilon}_z$.

At this stage is important to introduce the concept of effective stress, commonly found in soil mechanics [19]. Effective stress is defined as the difference between the total stress and the pore water pressure. Micromechanically it can be interpreted as the stress sustained by the elastic and friction forces between grains in contact. The Christoffersen's tensor [20, 21] calculates the effective stress tensor σ'_{ij}, from the components of the

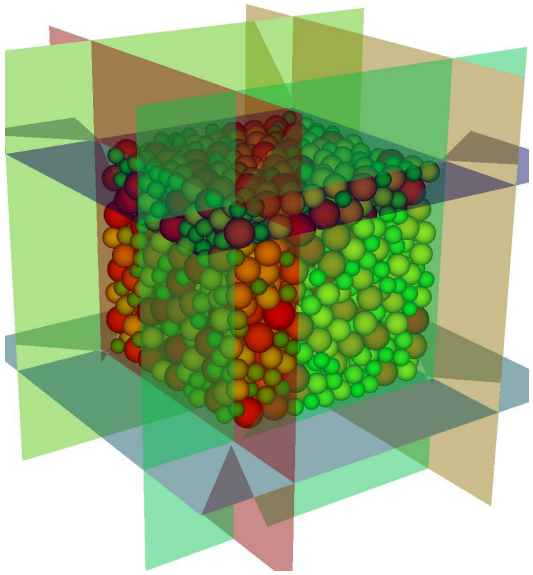

Figure 4. A triaxial test with different stresses applied on the walls.

contact forces f_i and the vector joining the pair's centers of mass b_j,

$$\sigma'_{ij} = \frac{1}{V} \sum_{\text{contacts}} f_i b_j, \tag{21}$$

where the summation is over all the contacts found in volume V. The contact forces include only the elastic and frictional forces and ignore the forces due to the pore water (Eq. 19) and therefore represent the effective stress over the grain fabric. With the definition of the effective stress tensor, the effective pressure p' (Eq. 1) and deviatoric stress q (Eq. 2) can be obtained from its principal values. It is worth noting that $q' = q$ whereas $p' \neq p$.

A critical implementation detail comes from the calculations of the pressure in the pores. When the pressure in Eq. 20 is considered locally at each cell, the sample becomes stiff, and it never fails. This can be seen in Fig. 5 where the q is shown as a function of ϵ_z. In a dry frictional soil, as in the case of $K_w = 0$, q eventually reaches a plateau signaling the soil failure. In contrast, for the case $K_w = 10$ MPa, the individual cells are not allowed to deformed enough due to the interlocking of the DEM particles. This interlocking at the cell level leaves little freedom for the DEM particles to be displaced relative to their neighbors. This problem is well known in FEA as the *volumetric locking* [16] and is produced by the reduced freedom the tetrahedral mesh possesses.

To solve this problem, it was found that the pressure should be calculated not over a single pore but over a subset of connected pores. The METIS library [22] was introduced to carry out this domain decomposition of neighbor pores. Firstly a graph was produced with nodes representing the individual cells and segments showing the

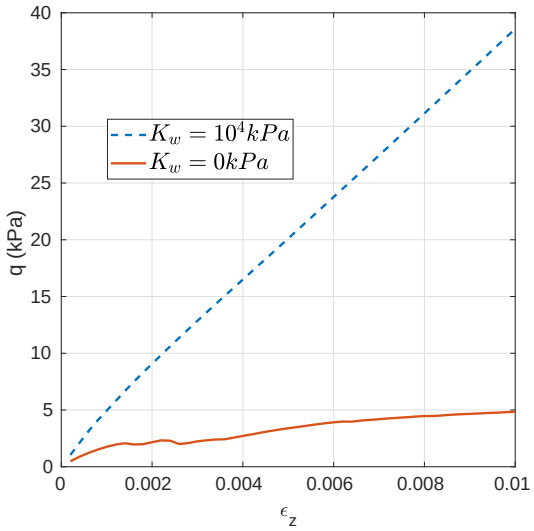

Figure 5. Deviatoric stress versus axial strain.

connectivity between neighbor cells. Then the METIS library was used to obtain a partition of this graph. Fig. 6 shows the partition algorithm which calculates the pressure of Eq. 20 for the subset of cells instead of the individual ones, characterized by the mean number of cells grouped in it N_c. This gives enough freedom for the system to allow shearing without extreme interlocking and still keeping the bulk pore volume constant.

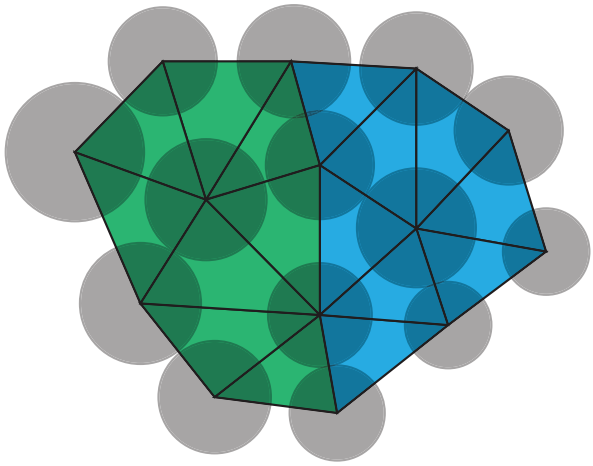

Figure 6. Partition of the cell set into two subsets for pressure calculation. The different colors represent two different partitions. The size of the partition is determined by the cell number N_c which for the case of the figure is equal to 8.

Different partitions were considered with a variable number of cells N_c in Fig. 7 where a q vs p' plot is introduced as in Fig. 1. As can be seen, introducing this partitions help to achieve the desired phenomenon where both p' and q decrease as the sample is sheared. The effect of N_c is significant with smaller values given larger growing rates for q. Eventually for the original case $N_c = 1$, q will grow unbound due to the interlocking described before. In contrast, larger values of N_c seem to reduce this trend. In all the cases considered, liquefaction is achieved, so a value of $N_c = 33$ was chosen for the remaining of this study. Future studies should consider N_c as a size of connected pores diffusing the water pressure u during the shearing time, in this way connecting this parameter with the soil hydraulic conductivity. An interesting conclusion from this observation is that for zero conductivity ($N_c = 1$) there is no liquefaction. When water is not allowed to leave one pore, the pressure produces particle interlocking, resisting shearing and increasing the soil strength.

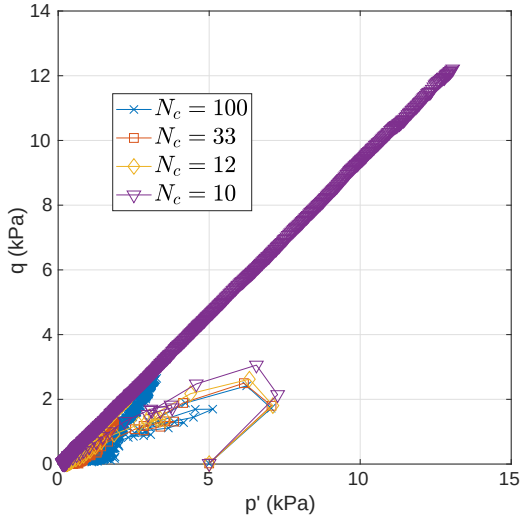

Figure 7. q versus p' for different values of the pore partition size N_c.

Once the partition size was determined, a second test was conducted to check the effect of the water bulk modulus K_w. Several values were considered ranging from $K_w = 0$ to $10MPa$. In Fig. 8 the sample volumetric strain is plotted against ϵ_z. This sample volumetric strain is calculated by adding the volume of each one of the tetrahedral cells for each time. This sample behaves like a loosely packed soil, subjected to an initial reduction of volume as it is sheared. However, as K_w increases, the tendency to contract is reduced. The maximum K_w value of $10MPa$ guarantees a very small volumetric strain on the order of 10^{-5} which is sufficient for the main goal to achieve a constant volume (up to a tolerance) under shearing. Further increments in K_w will just increase the precision, although, due to the explicit nature of the DEM, as the general stiffness of the system increases, smaller time steps will be needed for the numerical integration, greatly increasing computational time. As it will be shown later on, this is unnecessary since liquefaction can be reproduced from this model by ensuring this minimum volumetric strain. An important caveat

for this implementation is the comparison between the bulk modulus of the water and that of the grains. A good estimate of the Young modulus E of the grains is $E = \frac{K_g}{2R}$ [13] giving a value for the largest particle of $E = 55MPa$ which is larger than K_w. Also, the total deformation of the grains did not achieve values larger than 0.01% of the particle radius since this threshold was always monitored. It can be said then that the volumetric pore space deformation comes from the pores and not from the overlapping of the spheres.

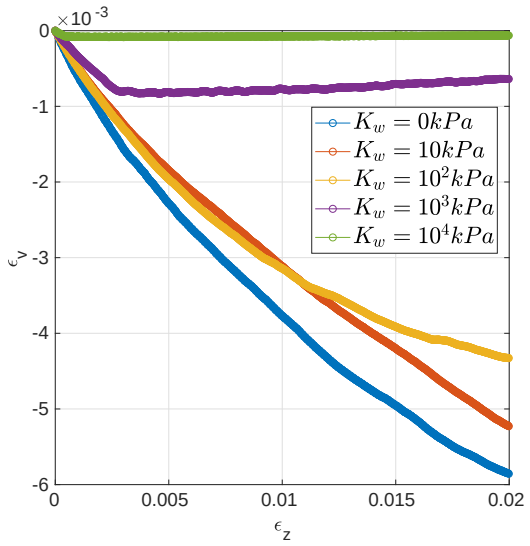

Figure 8. Sample volumetric strain versus axial strain.

Fig. 9 shows the q vs. p' plot for the different values of K_w. As can be seen, smaller values of K_w produce no liquefaction, with q growing in par with the total stress. Larger K_w values, where the sample volumetric strain is constrained to small values, show indeed the onset of liquefaction as described in Fig. 1. When the value of K_w is small, and the sample tends to contract, the grains increase their contacts by reducing the pore size increasing both p' and q. In contrast, when the volume change is kept small and the sample is loose, grains will lose contacts during shearing, reducing the overall soil strength. This is the micromechanical origin of soil liquefaction which will be further explored in the next section.

III. RESULTS FOR UNDRAINED SHEARING FOR DIFFERENT SAMPLE DENSITIES

Several soil samples were prepared with different densities. This was achieved by changing the friction coefficient during the isotropic compression stage (μ_0 lower than the friction coefficient during shearing μ). After this stage is over, the friction coefficient is fixed again to a value of 0.2, and then the sample is sheared. Fig. 10 shows the obtained behavior for the different initial friction coefficients. The effective pressure p' and deviatoric stresses q for all samples are compared with the total stress measured at the triaxial test walls. The results show that loosely packed sample ($\mu_0 = 0.2$), liquefies after a given deformation, whereas the densely packed one ($\mu_0 = 0.0$) increases its strength. Fig. 10 shows also graphically the value of the bulk pore pressure u_b, calculated as the difference between the total pressure at the triaxial test walls and p'. For all samples, u_b is negative initially, signalling dilation of the soil. At this stage the pore pressure force (Eq. 19) pulls the grains together, increasing the friction and the overall soil strength. However, the loose samples experience a transition where u_b changes sign, becoming positive and pushing the grains apart. This effect reduces the friction of the soil matrix and in turn, acts as the onset of a liquefaction event. Fig. 12 also shows the key characteristics displayed in Fig. 1, including the CSL envelope where all the trajectories converge. This proves that the model is capable of reproducing the liquefaction effect quantitatively.

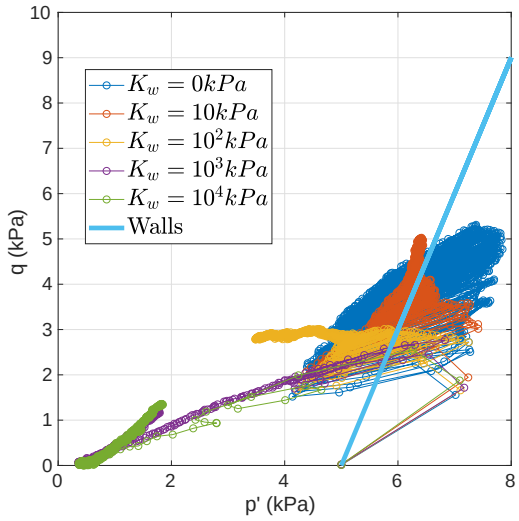

Figure 9. q versus p' for different values of the water bulk modulus K_w. The solid line represents the total p and q measured over the walls for comparison.

Soil liquefaction can be seen clearly by plotting the p' and q as a function of the axial strain ϵ_z in Figs. 11 and 12. As can be seen for the sample $\mu_0 = 0.2$, both p' and q reach a peak value at the beginning of shearing (before $\epsilon_z = 10^{-4}$) and then suddenly drop to negligible values. At this point, the pore pressure is equal to the total stress imposed on the triaxial test walls and the soil is providing no shear resistance. This behavior is contrasted with the dense soil ($\mu_0 = 0.0$) where both p_{eff} and q_{eff} keep increasing, despite some fluctuations. In these cases, pore water is actually increasing the soil strength and its shear stress resistance.

As mentioned in the introduction, dense and loose packings are still relative definitions, that still create a

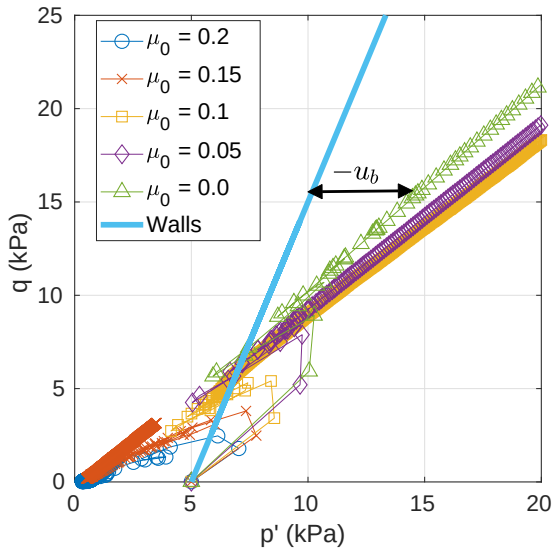

Figure 10. q versus p' for samples prepared with different initial coefficients μ_0. The solid line represents the total p and q measured over the walls for comparison.

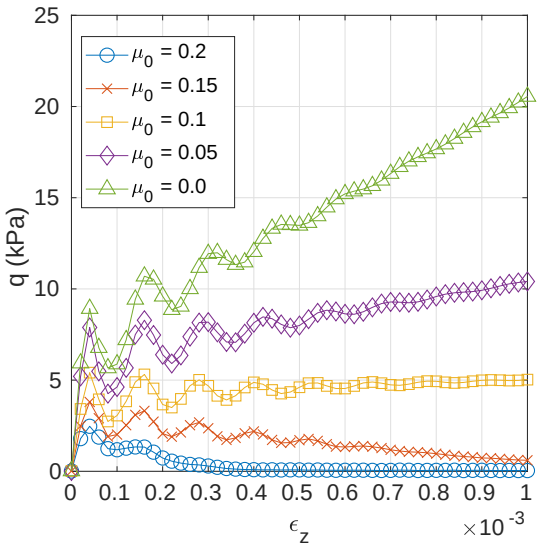

Figure 12. q versus axial strain.

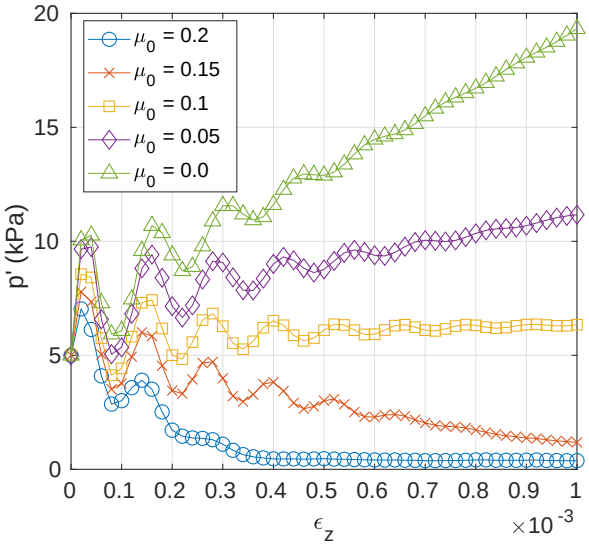

Figure 11. p' versus axial strain.

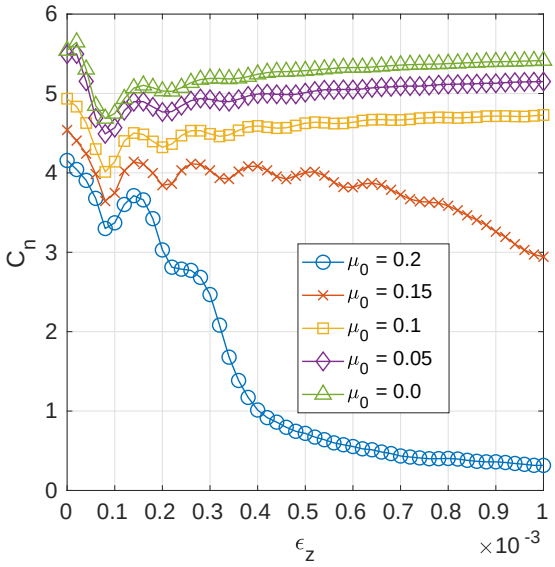

Figure 13. C_n versus axial strain.

significant difference on the onset of a liquefaction event. In order to analyse what happens with the solid skeleton, the evolution of the coordination number [23] C_n is studied. C_n is defined as the average number of contacts per particle. Fig. 13 shows that the samples have different initial C_n values ranging from 4 to 6. there seems to be a critical value between 4.5 and 5 differentiating samples that liquefy from the ones that gain shear strength. This critical value, which must depend on the soil size grading, acts as a bifurcation point separating both trajectories. The loose samples saw their granular skeletons destroyed, by particles having on average less than one contact, whereas in dense samples the granular skeleton structure remains consistent through the shearing process. In this preliminary study, the different initial values for C_n were achieved by changing μ_0 which is impossible to do in a real soil. In practice, liquefaction prevention is achieved by consolidation of the soil, which in some cases can be a lengthy process.

IV. CONCLUSIONS

A numerical method is introduced to simulate liquefaction in soils. Liquefaction occurs when the pore water resists compression, due to its high bulk modulus, exerting a repelling force over the grains and counteracting the contact and friction forces on the soil skeleton. When this happens, the soil is incapable of resisting shear stresses and it starts behaving like a fluid, hence the term liquefaction.

The proposed algorithm is based on the Discrete Element Method which is popular to study the micromechanics of granular materials. It models the individual mechanics of grains by means of simulating the contact and friction forces. The effect of water is introduced into the algorithm by diving the pore space into a Delaunay tessellation where the particles are positioned at the cells' nodes. Then forces opposing volume changes are applied to each cell. Once these forces are added to the contact and friction forces, the DEM particles' equations of motion are solved.

Initial testing showed that the constant volume constraint acted as a strong condition over individual cells. Liquefaction was obtained by grouping cells together and calculating the total volume change and pressure over these subsets. This was achieved by a graph decomposition algorithm ensuring that the subsets are formed from connected cells. A number of cells per partition $N_c = 3$ was chosen, although, as shown in Fig. 7, liquefaction was observed for a broad range of N_c values. N_c must be related to the characteristic time that the pressure takes to the diffused between connected pores, and hence, it is related to the hydraulic conductivity. An extension of this model could consider pressure diffusion to obtain a fully dynamic model.

Different samples were sheared under triaxial conditions with different initial densities. The initial density was controlled by changing the friction coefficient at the isotropic compression stage. It is shown that loose samples are susceptible to liquefy when the effective stress on them becomes zero during shearing. In this case, the pore pressure sustains to total stress imposed on the sample and the grains are suddenly floating without contacts. This does not occur on dense samples which are able to resist shearing and maintain their contact network through deformation.

To characterize this, the evolution of the coordination number C_n (average number of contacts per particle) was also observed. It is shown that there is a critical value of C_n differentiating a liquefaction event from a stable situation. Future studies should focus on the dependence of this critical C_n on the soil grain size distribution and grading.

[1] TG Sitharam, JS Vinod, and BV Ravishankar, "Post-liquefaction undrained monotonic behaviour of sands: experiments and dem simulations," Géotechnique **59**, 739–749 (2009).

[2] S. A. Galindo-Torres, D. M. Pedroso, D. J. Williams, and H. B. Mühlhaus, "Strength of non-spherical particles with anisotropic geometries under triaxial and shearing loading configurations," Granular Matter **15**, 531–542 (2013).

[3] Hai-Sui Yu, *Plasticity and geotechnics*, Vol. 13 (Springer Science & Business Media, 2007).

[4] P. A. Cundall and O. D. L. Strack, "A discrete numerical model for granular assemblages," Géotechnique **29**, 47–65 (1979).

[5] S Behraftar, SA Galindo Torres, A Scheuermann, DJ Williams, EAG Marques, and H Janjani Avarzaman, "A calibration methodology to obtain material parameters for the representation of fracture mechanics based on discrete element simulations," Computers and Geotechnics **81**, 274–283 (2017).

[6] Alex X Jerves, Reid Y Kawamoto, and José E Andrade, "A geometry-based algorithm for cloning real grains," Granular Matter **19**, 30 (2017).

[7] Ning Guo and Jidong Zhao, "The signature of shear-induced anisotropy in granular media," Computers and Geotechnics **47**, 1–15 (2013).

[8] Y. Wang, S. Abe, S. Latham, and P. Mora, "Implementation of Particle-scale Rotation in the 3-D Lattice Solid Model," Pure and Applied Geophysics **163**, 1769–1785 (2006).

[9] Fernando Alonso-Marroquín, Álvaro Ramírez-Gómez, Carlos González-Montellano, Nigel Balaam, Dorian A. H. Hanaor, E. A. Flores-Johnson, Yixiang Gan, Shumiao Chen, and Luming Shen, "Experimental and numerical determination of mechanical properties of polygonal wood particles and their flow analysis in silos," Granular Matter **15**, 811–826 (2013).

[10] SA Galindo-Torres and DM Pedroso, "Molecular dynamics simulations of complex-shaped particles using Voronoi-based spheropolyhedra." Physical review. E, Statistical, nonlinear, and soft matter physics **81**, 061303 (2010).

[11] W.F. Oquendo, J.D. Muoz, and A. Lizcano, "Oedometric test, bauer's law and the micro-macro connection for a dry sand," Computer Physics Communications **180**, 616 – 620 (2009), special issue based on the Conference on Computational Physics 2008.

[12] J. Cabrejos-Hurtado, S. Galindo Torres, and D.M. Pedroso, "Assessment of the mechanical behaviour of granular media by dem-based true triaxial tests," in *Advances of Computational Mechanics in Australia*, Applied Mechanics and Materials, Vol. 846 (Trans Tech Publications, 2016) pp. 428–433.

[13] N. Belheine, J.P. Plassiard, F.V. Donzé, and A. Darve, F.and Seridi, "Numerical simulation of drained triaxial test using 3D discrete element modeling," Computers and Geotechnics **36**, 320–331 (2009).

[14] S.A. Galindo-Torres, "A coupled discrete element lattice boltzmann method for the simulation of fluidsolid interaction with particles of general shapes," Computer Meth-

ods in Applied Mechanics and Engineering **265**, 107 – 119 (2013).
[15] The CGAL Project, *CGAL User and Reference Manual*, 4.12 ed. (CGAL Editorial Board, 2018).
[16] Johannes Catharinus Nagtegaal, David Moore Parks, and JR Rice, "On numerically accurate finite element solutions in the fully plastic range," Computer methods in applied mechanics and engineering **4**, 153–177 (1974).
[17] Olgierd Cecil Zienkiewicz, Robert Leroy Taylor, Olgierd Cecil Zienkiewicz, and Robert Lee Taylor, *The finite element method*, Vol. 3 (McGraw-hill London, 1977).
[18] GDR MiDia, "On dense granular flows," Eur. Phys. J. E **14**, 341–365 (2004).
[19] Muni Budhu, "Soil mechanics and foundations. john wley & sons," Inc. New York (2000).
[20] J Christoffersen, MM Mehrabadi, and Sia Nemat-Nasser, "A micromechanical description of granular material behavior," Journal of applied mechanics **48**, 339–344 (1981).
[21] Alex X Jerves and SA Galindo-Torres, "A microscale analytical study on the strength of two-dimensional frictional granular materials," International Journal of Geotechnical Engineering , 1–10 (2018).
[22] George Karypis and Vipin Kumar, "A fast and high quality multilevel scheme for partitioning irregular graphs," SIAM Journal on scientific Computing **20**, 359–392 (1998).
[23] Luigi La Ragione and Vanessa Magnanimo, "Contact anisotropy and coordination number for a granular assembly: A comparison of distinct-element-method simulations and theory," Physical Review E **85**, 031304 (2012).